



crystals

IMPACT
FACTOR
2.7

CITESCORE
3.6

Article

Study on the Effectiveness of Water Mist on Suppressing Thermal Runaway in LiFePO_4 Batteries

Qian Li, Jinshan Yu, Guangzhen Liu, Xiaoguang Ma, Wei Si, Xiangyu Hu, Guoqing Zhu and Tong Liu

Special Issue

Advances in Metal-Ion Batteries

Edited by

Dr. Maryam Sadat Kiai and Dr. Navid Aslfattahi



<https://doi.org/10.3390/cryst13091346>

Article

Study on the Effectiveness of Water Mist on Suppressing Thermal Runaway in LiFePO₄ Batteries

Qian Li ¹, Jinshan Yu ¹, Guangzhen Liu ¹, Xiaoguang Ma ¹, Wei Si ¹, Xiangyu Hu ², Guoqing Zhu ² and Tong Liu ^{2,*}¹ STATE GRID Tianjin Electric Power Company, Tianjin 300022, China² School of Safety Engineering, China University of Mining and Technology, Xuzhou 221116, China

* Correspondence: lt2022@cumt.edu.cn

Abstract: Lithium-ion batteries experience rapid temperature increases with a high risk of combustion and explosion during thermal runaway, and water mist has been considered as one of the most effective cooling strategies. The water mist field can be impacted by the safety valve airflow, subsequently affecting the cooling characteristics. In this paper, the water mist nozzle with a fixed working pressure is located 1 m above the 100 Ah LiFePO₄ battery to suppress the thermal runaway, and the cooling characteristics under various stages have been compared and analyzed. The results show that the development of thermal runaway can be inhibited before thermal runaway is initiated, and the water mist presents a better cooling effect after the battery safety valve is opened. The critical accumulation heat density of 155 kJ/kg has been identified, which is the threshold for thermal runaway suppression. The confrontation between water mist and the flame has been analyzed, and the water mist droplets cannot fall on the battery surface, resulting in a poor cooling rate of 0.57 kW. This means the suppression effect of water mist will be affected by the airflow impact of the safety valve.

Keywords: LiFePO₄ battery; thermal runaway; water mist; accumulated heat density; confrontation phenomenon



Citation: Li, Q.; Yu, J.; Liu, G.; Ma, X.; Si, W.; Hu, X.; Zhu, G.; Liu, T. Study on the Effectiveness of Water Mist on Suppressing Thermal Runaway in LiFePO₄ Batteries. *Crystals* **2023**, *13*, 1346. <https://doi.org/10.3390/cryst13091346>

Academic Editor: Andreas Thissen

Received: 17 August 2023

Revised: 27 August 2023

Accepted: 28 August 2023

Published: 4 September 2023



Copyright: © 2023 by the authors. Licensee MDPI, Basel, Switzerland. This article is an open access article distributed under the terms and conditions of the Creative Commons Attribution (CC BY) license (<https://creativecommons.org/licenses/by/4.0/>).

1. Introduction

In the context of the worldwide drive to promote the use of electric energy, lithium-ion batteries are the primary option for storing chemical energy because of their durability, high energy density, and low environmental impact [1]. Currently, the commonly employed lithium-ion batteries include lithium cobalt-acid batteries, lithium manganese-acid batteries, lithium nickel-cobalt-manganese-acid batteries, and lithium iron phosphate batteries [2]. Of these, LiFePO₄ batteries are extensively applied in electric vehicles and energy storage due to their favourable characteristics such as long lifespan, low cost, and high safety levels [3].

A lithium-ion battery is primarily composed of a positive electrode, a negative electrode, a separator, a positive electrode collector, a negative electrode collector, and an electrolyte. Owing to the significant number of active materials inside and the high energy density, lithium-ion batteries exhibit irreversible thermal runaway when exposed to external conditions of overcharging, overheating and puncturing [4]. In the event of thermal runaway, the active materials inside the battery undergo intense pyrolysis reactions that generate a substantial amount of heat and flammable toxic gases [5]. These gases consist of electrolyte vapours as well as other flammable gases including hydrogen, carbon monoxide, methane and ethylene [6]. The battery is susceptible to violent jet fires after a thermal runaway event due to rapid gas production and high internal temperatures. This can cause thermal runaway to spread to neighbouring batteries and transfer the heat [7]. The thermal runaway characteristics of lithium-ion batteries depend heavily on the material used for the positive electrode. According to Doughty and Pesaran [8], lithium iron phosphate exhibits the best thermal stability and the highest thermal decomposition temperature

(over 240 °C), followed by lithium manganate (220 °C), lithium nickel cobalt manganate (200 °C) and lithium cobaltate (200 °C). The thermal runaway characteristics of the battery are also directly affected by its state of charge (SOC). Zhang et al. [9] found that as the SOC increases, the thermal runaway phenomenon of the battery becomes more severe, and high SOC batteries have a higher risk of thermal runaway combustion. Ma et al. [10] found that the gas production and production rate of 18650 Li-ion ternary batteries with 100% SOC are about 1.8 times and 6 times that of 50% SOC, respectively, and the risk of thermal runaway combustion of batteries with high SOC is higher.

Due to its high temperature rise rate, heat release rate, and generation of jet fire, the thermal runaway of lithium-ion batteries is currently suppressed mainly by the two aspects of pre-runaway control and post-runaway cooling. Li Yi et al. [11] researched the effectiveness of extinguishing agents including dry powder, carbon dioxide and aqueous film-forming foam, all of which were found to suppress battery flames, but potentially cause re-ignition. Rao Hui et al. [12] explored the suppression effects of carbon dioxide, HFC-227ea and hot aerosol, discovering that battery fires can re-ignite after instantaneous extinguishing. Among these, hot aerosol had the poorest cooling effect and the shortest re-ignition interval. In their study, Xu et al. [13] examined the effectiveness of carbon dioxide, HFC-227ea, and water mist as extinguishing agents. They reported that carbon dioxide and HFC-227ea had poor cooling effects and the fire tended to re-ignite after extinguishing, whereas water mist exhibited the most effective cooling effect. Zhang et al. [14] compared the cooling effects of water mist with carbon dioxide, HFC-227ea, and $C_6F_{12}O$. They reported that $C_6F_{12}O$ exhibited a poor cooling effect when used alone, but it showed the best cooling effect when used together with water mist. Furthermore, according to Zhang [15], water spraying can only delay the onset of thermal runaway, but cannot prevent its propagation. This process would lead to an increase in the concentration of carbon monoxide, hydrogen, and hydrogen fluoride, while decreasing the amount of carbon dioxide. Liu et al. [16–18] noted that water mist can serve as an effective inhibitor of thermal runaway before reaching the critical control temperature, as well as extinguish flames and mitigate damage under overcharge conditions, thanks to its superior cooling ability. Furthermore, water mist can effectively prevent the propagation of thermal runaway. Li et al. [19] found that the addition of 1.0% NaCl, 1.5% SDBS and 0.5% protein to water mist could improve the cooling and thermal runaway inhibition effect. According to the study by Liu [20], the synergistic use of $C_6F_{12}O$ and water mist could significantly reduce the peak temperature and high temperature duration of thermal runaway compared to $C_6F_{12}O$ alone. Furthermore, the effectiveness of cooling inhibition in the water mist could be improved by adding $KHCO_3$ and $K_2C_2O_4 \cdot H_2O$ to it.

Current research indicates that water mist is among the most effective cooling strategies. Water acts as the cooling medium, and small droplets quickly evaporate to absorb heat after encountering high temperatures without affecting the cooling effect by accumulating on the surface. In addition, water mist requires comparatively less water to extinguish a fire and reduces the likelihood of short-circuiting by not submerging the battery. However, water mist nozzles are typically closer to the batteries in most of the current studies. The initiation of thermal runaway accelerates gas production in the battery, and the rate of gas jet from the safety valve is increased. Being too close ignores the confrontation of the safety valve gas flow with the water mist. Hence, this study increases the distance between the water mist nozzle and the battery safety valve to 1 m. By observing the cooling characteristics and fire extinguishing phenomenon during the inhibition process, it investigates the effectiveness of water mist when inhibiting the thermal runaway of $LiFePO_4$ batteries under this distance.

2. Experimental Design

2.1. Battery Samples

The experiments utilized square aluminium-cased LiFePO₄ batteries with graphite as the negative electrode material. Each battery had a nominal capacity of 100 Ah, an individual mass of 1980 g and dimensions of 2160 mm × 1350 mm × 35 mm. Additionally, the batteries had a maximum cut-off voltage of 3.6 V and a minimum cut-off voltage of 2.5 V. Prior to the experiment, each battery sample had undergone two cycles on the Neware charge/discharge cycler and was charged to 100% state of charge (SOC) for experimental consistency.

2.2. Experimental Set-Up

Figure 1a shows that the test bench was constructed in accordance with the ISO9705 standard. The bench was constructed of stainless-steel plates. The upper part contained a fume hood that discharged exhaust gas through a ventilator. Additionally, there was a side panel with a high-temperature tempered glass observation window. The bottom was elevated with a water supply pipe and nozzle connection port reserved in the inner part. Prior to beginning the experiment, the battery module was placed inside the combustion chamber. Additionally, a DV recorder was positioned beyond the observation window to observe experimental phenomena. Once the battery reached the cooling condition, the fire extinguishing agent was immediately sprayed through the reserved pipe and nozzle.

As shown in Figure 1b, the battery module consisted of a steel fixture, two heat-insulation plates, a heating plate, a stress sensor and a battery. The contact area between the copper heating plate and the battery measured 2160 mm × 1350 mm. The heating switch and power were controlled by a control panel and preset to 400 W. The stress sensor measured 150 mm × 150 mm × 24 mm and had an integrated error of ±0.1~0.3% F.S. All the batteries had their external plastic rubber skin removed prior to the experiment. The location of the thermocouples is depicted in Figure 1c; they were placed in the middle of the unheated side of the experimental battery and 1 cm, 10 cm, 20 cm, 30 cm, 50 cm, 70 cm, 90 cm above the safety valve, with a diameter of 1.5 mm, a length of 3000 mm, a temperature measurement range of −100 °C~1200 °C, a measurement accuracy of ±1.5~5 °C, and a recording frequency of 1 Hz. An electronic scale was placed under the battery module to measure the mass, with a measurement range from 0 kg to 30 kg. Three types of data were monitored in the experiment: temperature data was collected using type K armoured thermocouples, stress data was collected using stress sensors, and mass data was collected in real time using electronic scales. The water mist nozzle had a working flow rate of 400 mL/min, and a design working pressure of 6 MPa. It was installed 1 m above the battery safety valve.

2.3. Cases Setting

Two aspects were explored in the experiment: first, we aimed to determine if the water mist could cool and inhibit the thermal runaway initiation of the battery; second, we aimed to assess the effectiveness of the mist in cooling and inhibiting thermal runaway of the battery. This study was designed with seven groups of cases, as presented in Table 1, to account for different stages before and after thermal runaway. Based on the most adverse condition principle, the battery SOC was set to 100% to observe the inhibition effectiveness of the water mist. As shown in Figure 2, based on the thermal runaway process in Case 1, it can be inferred that the battery temperature was 108 °C when the safety valve was open, 140 °C when the thermal runaway was initiated, and the maximum temperature of the thermal runaway was about 400 °C. In Cases 2~4, we aimed to investigate how water mist inhibited thermal runaway at different stages. Meanwhile, in Case 5 we aimed to investigate the effect of heating rate on the inhibition results. In Cases 6 and 7 we aimed to investigate the inhibition effect of cooling with water mist at different stages after thermal runaway.

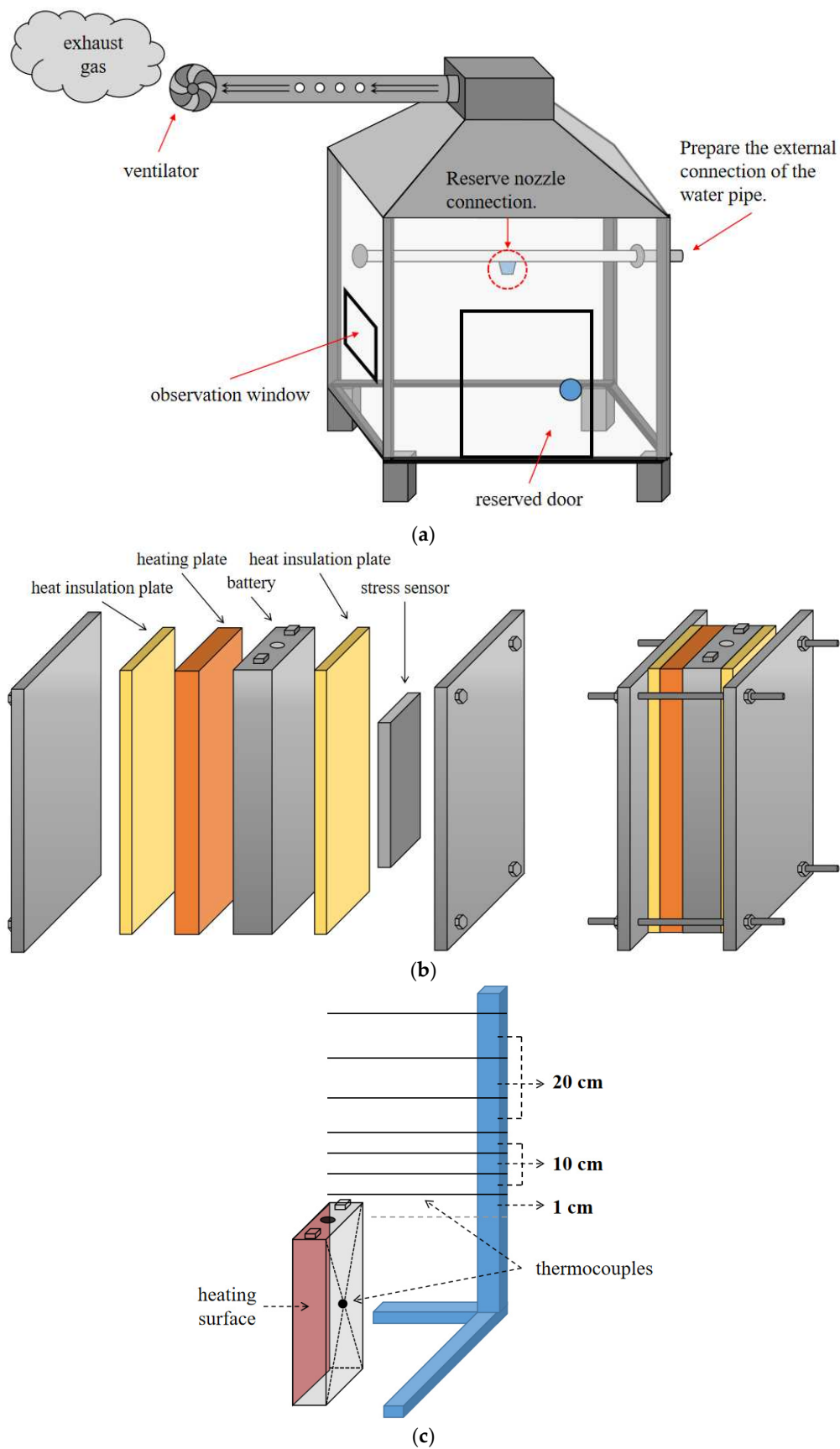
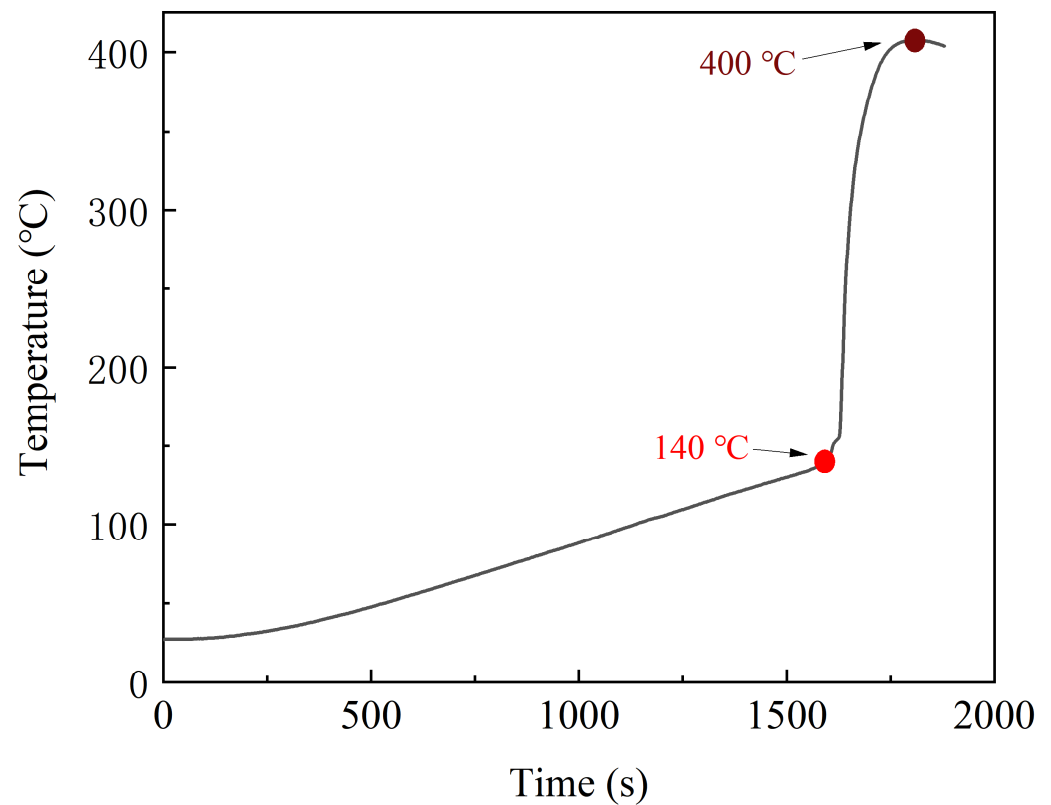


Figure 1. Experimental setup: (a) schematic diagram of experimental bench; (b) schematic diagram of the battery module; (c) thermocouple layout.

Table 1. Cases settings.

No.	SOC	Water Mist Release Temperature	Description of Cases
Case 1	100%	\	non-extinguishable
Case 2	100%	80 °C	safety valve not open
Case 3	100%	108 °C	extinguish the fire as soon as the safety valve is opened
Case 4	100%	~116 °C	extinguish the fire 3 min after opening the safety valve
Case 5	100%	~107 °C	extinguish the fire 3 min after opening the safety valve, 1.5 times the heating power
Case 6	100%	140 °C	extinguish fire immediately after thermal runaway
Case 7	100%	400 °C	cooling after thermal runaway maximum temperature

**Figure 2.** Battery thermal runaway temperature curve in Case 1.

The experimental equipment and battery modules were assembled and debugged before the experiments, and the stress, temperature, mass recording and heating were initiated at the same time as the experiment started, and the video recorder was turned on after 5~15 min, depending on the cases. The smoke exhaust ventilator was activated after the water mist release stopped. Depending on the cases, the heating was stopped after the water mist release stopped or the battery thermally overheated. The data loggers and water mist were turned off after each critical point was recorded, and then the experiment was terminated.

3. Experimental Results and Analyses

3.1. Analysis of Water Mist Cooling

When subjected to continuous heating, Lithium-ion batteries will gradually experience self-heating, safety valve opening and eventually thermal runaway. During this process, the battery will generate a significant amount of heat spontaneously. If not cooled promptly, the thermal runaway could spread to other batteries, creating a substantial fire hazard. Equation (1) can be used to calculate the heat accumulation of the battery itself after spontaneous heat generation.

$$Q_{rem} = Q_{tot} - Q_{air} \quad (1)$$

where, Q_{rem} is the remaining heat of the battery; Q_{tot} is the total heat transferred by the battery self-heating and the heating plate; Q_{air} is the heat dissipated by the air.

Q_{rem} and Q_{air} can be calculated by Equations (2) and (3), respectively.

$$Q_{rem} = c_b m_e (T_e - T_0) \quad (2)$$

$$Q_{air} = Ah \int_0^T (T_i - T_a) dt + A \varepsilon \sigma \int_0^T (T_i^4 - T_a^4) dt \quad (3)$$

where, c_b is the specific heat of the battery, which is assumed to be uniform throughout the calculation and is assigned a value of 1.38 kJ/(kg·K); m_e is the remaining mass of the battery; T_0 and T_e are the temperature of the battery at the beginning and the end of the experiment, respectively; A is the area of the battery exposed to the air; h is the air convection heat transfer coefficient, assuming the air is naturally convective in the experimental and taking the value of 10 W/(m²·K); T is the total experimental time; T_i and T_a are the battery temperature at time i and ambient temperature, respectively; ε is the surface emissivity of the battery, which takes the value 0.05 because the battery surface is a smooth aluminium surface [21]; σ is the Stefan-Boltzmann constant, which takes the value of 5.67×10^{-8} W/(m²·K).

Q_{rem} and Q_{air} can be derived from the calculation, which can be substituted into Equation (1) to calculate Q_{tot} at each moment of cut-off in Case 1. Taking the safety valve opening time as a reference, then the total heat production of different cases can be calculated. When cooling inhibition is intervened, the heat of water mist cooling Q_{WM} can be calculated by Equation (4).

$$Q_{WM} = Q_{tot} - Q_{rem} - Q_{air} \quad (4)$$

The opening of the battery safety valve causes gas to be ejected from the battery; this heat loss Q_{eje} will be discussed below.

Assuming the distributions of stress, electrolyte and gas production within the battery after self-generated heat are uniform, and ignoring the effect of potential energy, the fluid ejected from the safety valve is assumed to satisfy Bernoulli's law as shown in Equation (5).

$$P = \frac{1}{2} \rho v^2 \quad (5)$$

where, P is the pressure inside the battery; ρ is the density of the gas ejected from the safety valve; v is the flow rate of the gas ejected from the safety valve.

Derived from the above equation, the mass of gas ejected from the battery safety valve M_{val} is proportional to the integral of the square root of the battery stress F . The amount of heat Q_{eje} , carried away by the gas ejected after the safety valve is opened can be calculated from Equation (6).

$$Q_{eje} = c_b M_{val} \Delta T = \alpha c_b \int_0^T \sqrt{F} dt \int_0^T (T_i - T_1) dt \quad (6)$$

where T_1 and T_i are the temperature at the safety valve before the safety valve is opened and the battery temperature at time i , respectively; T is the total time of the experiment; α is a constant calculated from the experiment data and has the value 3.8×10^{-5} .

Therefore, when the safety valve is opened, the heat of water mist cooling Q_{WM} can be calculated by Equation (7).

$$Q_{WM} = Q_{tot} - Q_{rem} - Q_{air} - Q_{eje} \quad (7)$$

The mass data for Case 1 is plotted and fitted as shown in Figure 3. After the safety valve is opened, there are two drop intervals in the battery mass, corresponding to the two times when the safety valve is opened and the thermal runaway is initiated. In the first drop interval, the battery is observed to be overweight due to the reaction force of the ejected gas on it when the safety valve is relieved. During the second drop interval, it is observed that the rate of mass loss is greater in the first half and the mass is more stable in the other half. The findings suggest that the electrolyte evaporates faster and the side reactions are more intense after the thermal runaway is initiated; when the electrolyte is exhausted, the battery mass tends to stabilize and the thermal runaway process tends to end. The ExpAssoc function model has been used to fit the two drop intervals, both of which gives a correlation index R^2 greater than 0.95. The high confidence level of the fit suggests that the battery mass loss is stable without serious fluctuations and could be applied to the above equation calculations.

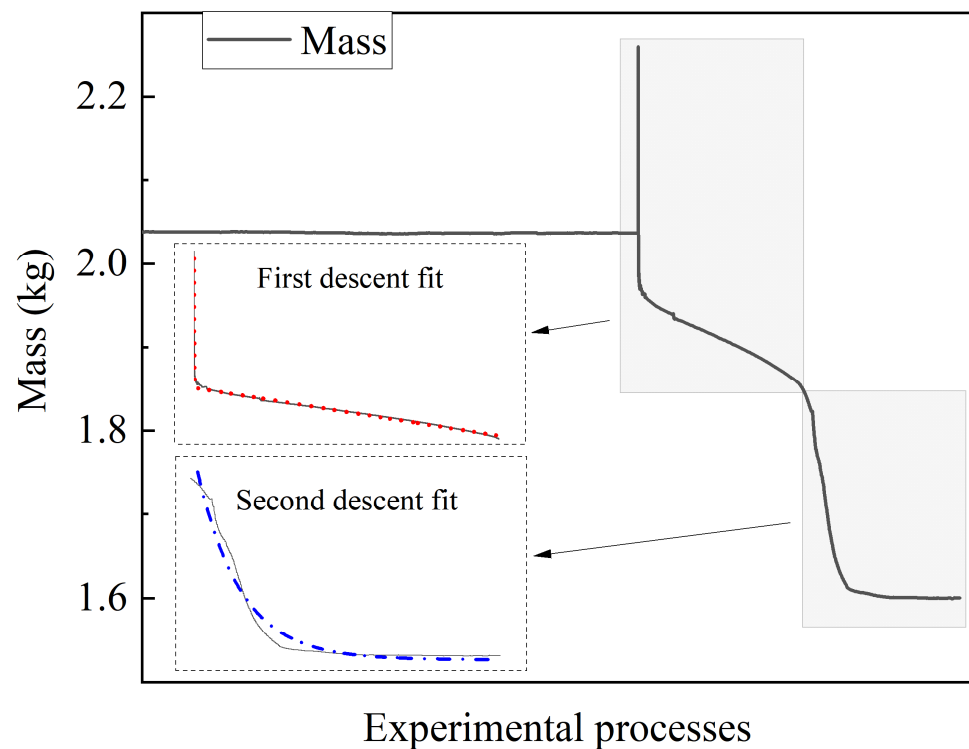


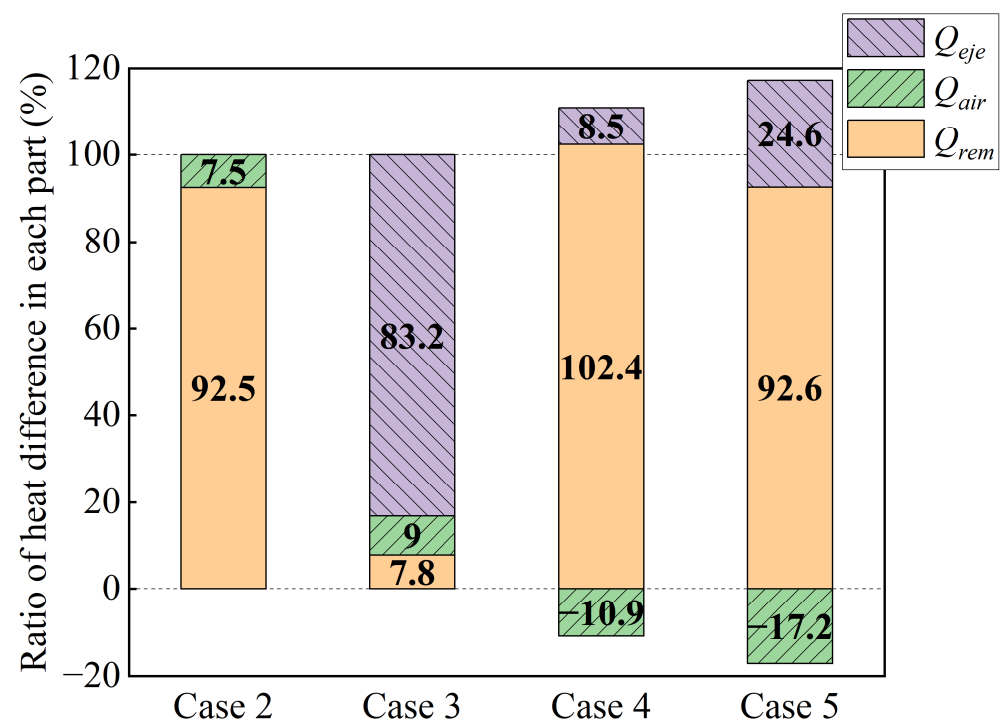
Figure 3. Battery mass curve. (The red line represents the fitted curve for the first mass descent and the blue line represents the fitted curve for the second mass descent).

By inputting the experiment data of each case into the calculation, as well as the water mist release time, we can derive the heat and water mist cooling rate of each part of each case, as shown in Table 2.

Table 2. Statistics of heat and water mist cooling rate of each part of each case.

No.	Q_{rem} (kJ)	Q_{tot} (kJ)	Q_{air} (kJ)	Q_{eje} (kJ)	Q_{WM} (kJ)	Cooling Rate (kW)
Case 1	841.6	993.8	27.6	124.6	\	\
Case 2	197.8	229.9	9.6	\	22.5	0.08
Case 3	228.8	250.8	11.6	0.1	10.3	0.80
Case 4	220.4	266.6	16.2	17.0	13.1	1.09
Case 5	209.5	257.7	9.0	12.0	27.3	1.52
Case 6	173.6	1058.7	113.7	191.1	580.3	0.36
Case 7	184.7	1033.1	133.5	122.8	592.1	0.34

The cooling rates of Cases 3 to 5 are 0.80 kW, 1.06 kW and 1.52 kW, respectively, which are higher than that of Case 2 (0.08 kW), indicating that the cooling rate of water mist release is higher after the safety valve of the battery is opened, i.e., the heat transfer effect between the water mist and the jet gas is more effective when the water mist and the jet gas are convected. Using the safety valve opening and thermal runaway initiating time point of Case 1 as the basis, the corresponding Q_{tot} for each case from the start of heating to the end of extinguishing can be calculated. On the assumption that the batteries underwent the same thermal runaway process in each case, the heat difference of each part affected by the water mist can be derived by subtracting the heat of each part in Cases 2 to 5 from the corresponding stage in Case 1, as shown in Figure 4. The main role of the water mist cooling part is: Cases 2, 4 and 5 mainly Q_{rem} , accounting for 92.5%, 102.4%, and 92.6%, respectively; Case 3 mainly Q_{eje} , accounting for 83.2%. It is noticed that there are cases where the percentage heat difference is greater than 100%. This is due to the fact that water droplets reduce the temperature on the surface of the battery, and this reduction affects the convective and radiative heat transfer with the air, making the Q_{air} difference negative. The percentage of heat difference indicates that when the battery is violently ejected, the water mist cooling mainly works to suppress the ejected heat, but otherwise mainly works to reduce the temperature of the battery itself. As there is a component of water mist cooling after reaching the highest temperature during thermal runaway in Cases 6 and 7, further analyses will be conducted separately in the following section.

**Figure 4.** Ratio of heat difference in each part of the battery for Cases 2~5.

Prior to the release of water mist, the temperature rise rate of the battery increases over 400 s and stabilizes after 400 s. The temperature rise rates of Cases 2~4 are about 0.07 °C/s and that of Case 5 is about 0.11 °C/s. Following the release of the water mist, the temperature rise rate reduces differently in each case, of which Case 3 decreases the most, and the duration of battery fire extinguishing of Cases 3~5 is similar, which is about 15 s. This is because the heat storage of the battery is less and the self-produced heat rate is slower before the onset of thermal runaway, which means that the main reason for the battery temperature rise is still the heat transfer from the heating plate. At this time, the application of water mist cooling can inhibit the battery temperature rise. After the application of water mist cooling, the temperature of the battery in Cases 2~5 remains stable before and after the time of thermal runaway initiation in Case 1. Cases 2 and 3 remain stable at about 100 °C, while after a longer heating time in Cases 4 and 5, the battery temperature remains stable at about 120 °C. The accumulated heat density is introduced and its calculation is shown below in Equation (8).

$$\dot{Q} = c_b(T_i - T_0) \quad (8)$$

where c_b is the specific heat of the battery, which is assumed to be uniform throughout the calculation and is assigned a value of 1.38 kJ/(kg·K); T_0 and T_i are the battery temperatures at the start of heating and at any time i , respectively.

The critical accumulated heat density for thermal runaway is noted at 155 kJ/kg for the battery in Case 1 at the onset of thermal runaway. As shown in Figure 5, after the water mist is released, the increase in the accumulated heat density in Cases 2, 4 and 5 immediately slows down, and after a period, the increase gradually stops and turns into a downward trend; while in Case 3, the accumulated heat density of the battery immediately decreases after the water mist is released. Clearly, the small-diameter water droplets falling on the battery surface could immediately evaporate and absorb the heat, and will not form a water film on the battery surface which could affect the subsequent droplet evaporation to dissipate the heat. Before and after water mist cooling, the maximum accumulated heat density of the batteries in Cases 2~5 is 108 kJ/kg, 120 kJ/kg, 124 kJ/kg and 124 kJ/kg, respectively, which is less than the critical value of 155 kJ/kg. In conclusion, the release of water mist before the onset of thermal runaway is effective in suppressing the thermal runaway of the batteries.

For Case 6, since the release of water mist occurs at the initiation of thermal runaway, the cooling process of water mist should be divided into two stages: inhibition before and cooling after the end of thermal runaway, and the cut-off point is at the moment when the battery reaches its maximum temperature. Applying the equation above, the value of Q_{rem} , Q_{tot} , Q_{air} , Q_{eje} and Q_{WM} is 756.2 kJ, 1058.7 kJ, 29.0 kJ, 191.1 kJ and 82.4 kJ, respectively in the first stage, and the cooling rate of the water mist is 0.78 kW. Compared to this stage of Case 1, Q_{rem} decreases by 150.3 kJ and Q_{air} and Q_{eje} increases by 12.0 kJ and 66.5 kJ, respectively in the first stage of Case 6, indicating that the heat accumulated inside the battery decreases and the heat ejected from the battery increases. Figure 6 shows that the thermal runaway initiation time is delayed by 231 s compared to Case 1. This delay allows more heat to accumulate inside the battery, resulting in a more intense thermal runaway process and more heat being removed by the gas jet. It can be deduced from the fact that the maximum surface temperature of the thermal runaway battery increases by almost 15 °C and the average temperature of the battery safety valve increases by almost 140 °C. The duration of thermal runaway in Case 6 is nearly 80 s less than in Case 1. Since the above thermal runaway process is more intense, it could be considered that although the water mist cannot reduce the thermal runaway of the battery, it can reduce the total duration of thermal runaway, thus reducing the loss due to thermal runaway of the battery. As the cooling rate is slightly lower in the first stage of Case 6 than in Cases 2~5, and there is an obvious confrontation and delamination phenomenon between the water mist and the battery flame in the experiment, it could be inferred that this phenomenon is the

reason for the slightly lower cooling rate of the water mist, which will be analysed in the following sections.

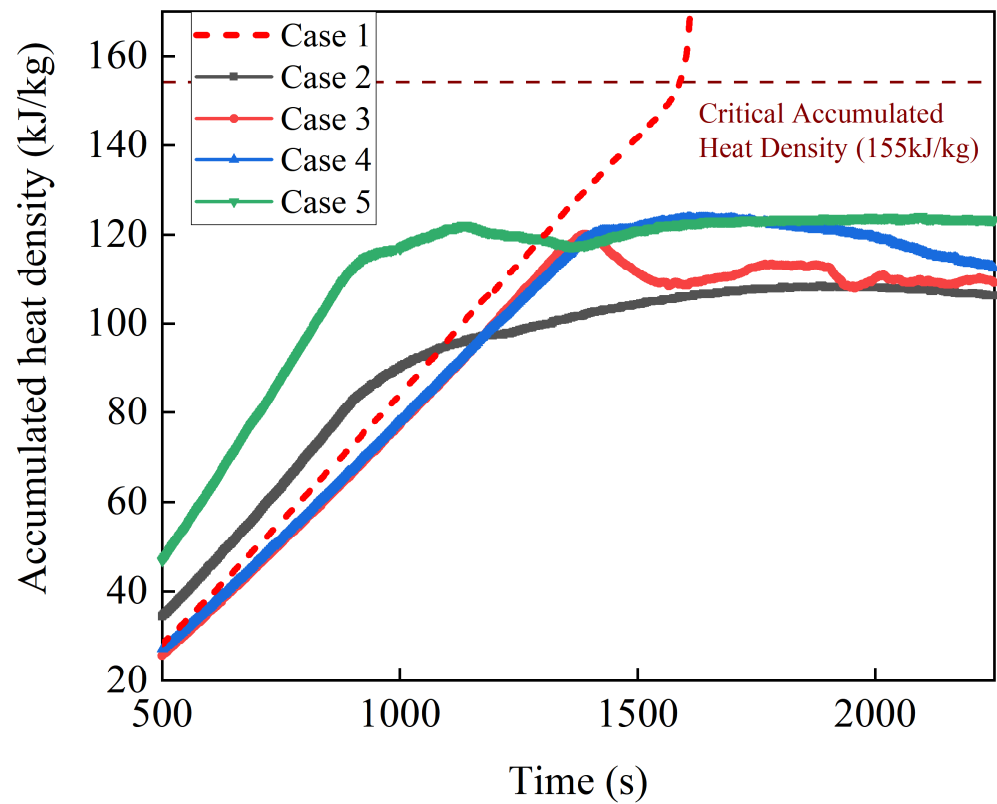


Figure 5. Variation curves of accumulated heat density of cells in Cases 2~5. (The dark red horizontal line represents the critical accumulated heat density).

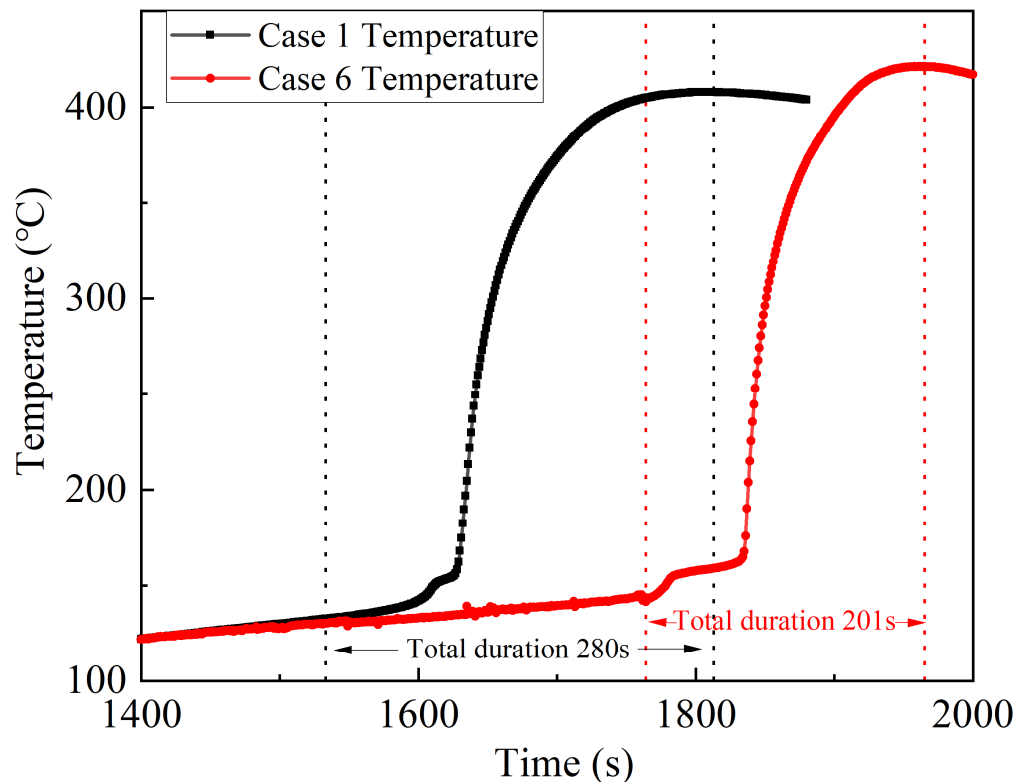


Figure 6. Variation curves of thermal runaway temperature of batteries in Cases 1 and 6.

During the second stage of Case 6, the thermal runaway of the battery ceases and it no longer produces heat by itself, and at this time the water mist cooling all acts on the remaining heat of the battery. Subtracting the total Q_{WM} of Case 6 from that of the first stage, the Q_{WM} of the second stage is 498.0 kJ, which can be calculated as a cooling rate of 0.33 kW, and that of Case 7 is 0.34 kW. According to Figure 7, Case 6 has a shorter actual cooling time, and the time required to cool the battery to 100 °C is reduced by 295 s compared to Case 7. There is no significant difference between the cooling rate of Cases 6 and 7 when the battery temperature is above 225 °C; when the battery temperature drops to 225 °C, the cooling rate of Case 6 increases significantly and is much higher than that of Case 7. This is because in Case 6, water mist is released at the onset of thermal runaway, which leads to cooling throughout the entire process of the battery thermal runaway. While the violent thermal runaway cannot be suppressed, the continuous cooling can shorten the duration of the thermal runaway. Coupled with the higher cooling rate and shorter cooling time at the location shown in Figure 7a in the second stage of Case 6, it could be inferred that when the thermal runaway ceases, the internal temperature of the battery is lower than that in Case 7. Since the internal temperature of the battery during thermal runaway is much higher than the surface, there is a certain delay when using surface temperature to judge the trend of internal temperature. The significant ‘dive’ in the battery temperature curve when the temperature decreases to 225 °C, compared to Case 7, reflects the lower internal battery temperature in Case 6.

The violent pyrolytic reaction between the electrolyte and the cathode material will generate a large amount of heat during the thermal runaway of the battery [22]. The internal structure of the battery is irreversibly damaged when the separator melts, which directly lead to the initiation of the thermal runaway [23]. In other words, the collapse and melting of the separator directly causes the reaction between the electrolyte and the cathode material. From Figure 8, it is clear that the three parts of each curve can well match the three stages of the accumulative heat density increase of the thermal runaway process in lithium ion batteries: the first stage of the SEI film pyrolysis corresponds to the slowly rising part of the curve; the second stage of the separator collapse and melting corresponds to the jumping part of the curve; and the third stage of the violent reaction between the anode and cathode material corresponds to the rapidly rising part of the curve. It should be noted that the melting of the separator is a rare endothermic reaction during the thermal runaway process, which corresponds to the decline in the slope of the curve in the second stage of the process. During the process of melting, the PE separator has a heat absorption of 190 J/g, while the PP separator has a heat absorption of 90 J/g [24]. When the separator starts to melt, the pyrolysis reactions inside the battery are intensified, so the slope of the curve at the beginning of the second stage is higher than that of the first stage. Upon the large-scale melting of the separator, the heat absorption rate increases and the slope of the curve decreases significantly until the separator is melted. The thermal runaway process could not be prevented in the second stage due to the irreversible damage to the internal structure of the battery, even if Case 6 intervened with water mist for cooling. Hence, the critical heat density accumulation of 155 kJ/kg at the initiation of the second stage is identified as the critical point to determine whether the initiation of thermal runaway can be inhibited.

In conclusion, water mist performs well in cooling and preventing thermal runaway when the battery has not initiated thermal runaway yet. When reaching the second stage of thermal runaway process, the battery separator starts to melt, then the application of water mist could not be able to inhibit the occurrence of thermal runaway, but it can reduce the duration of thermal runaway and the cooling time required after it happens, thus reducing the loss caused by thermal runaway of the battery.

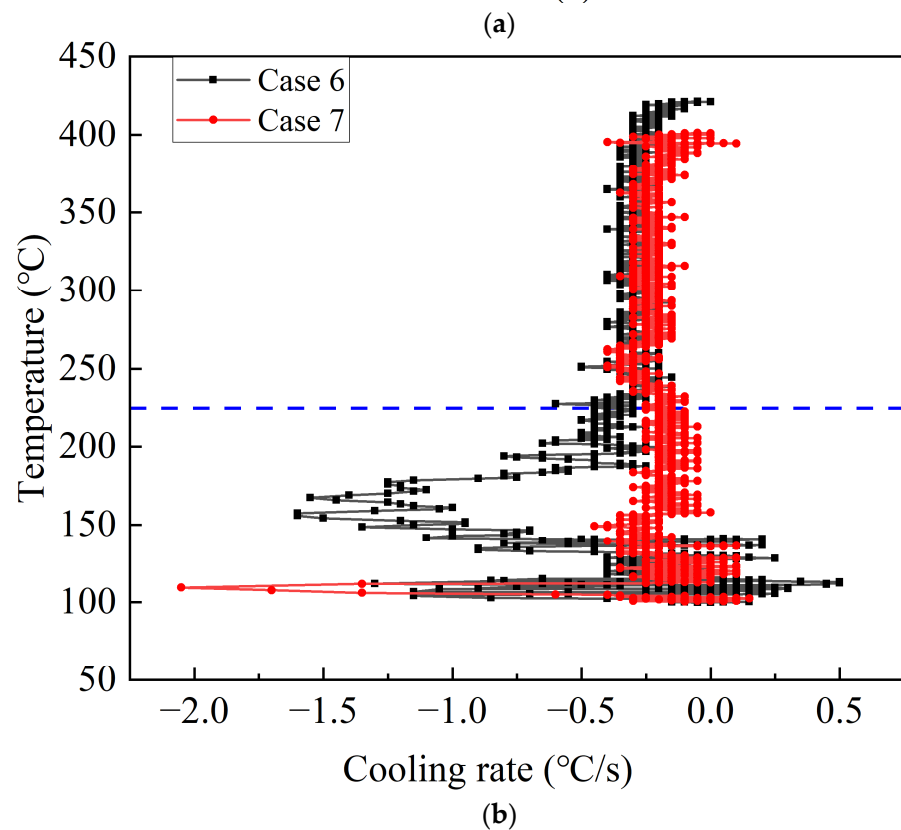
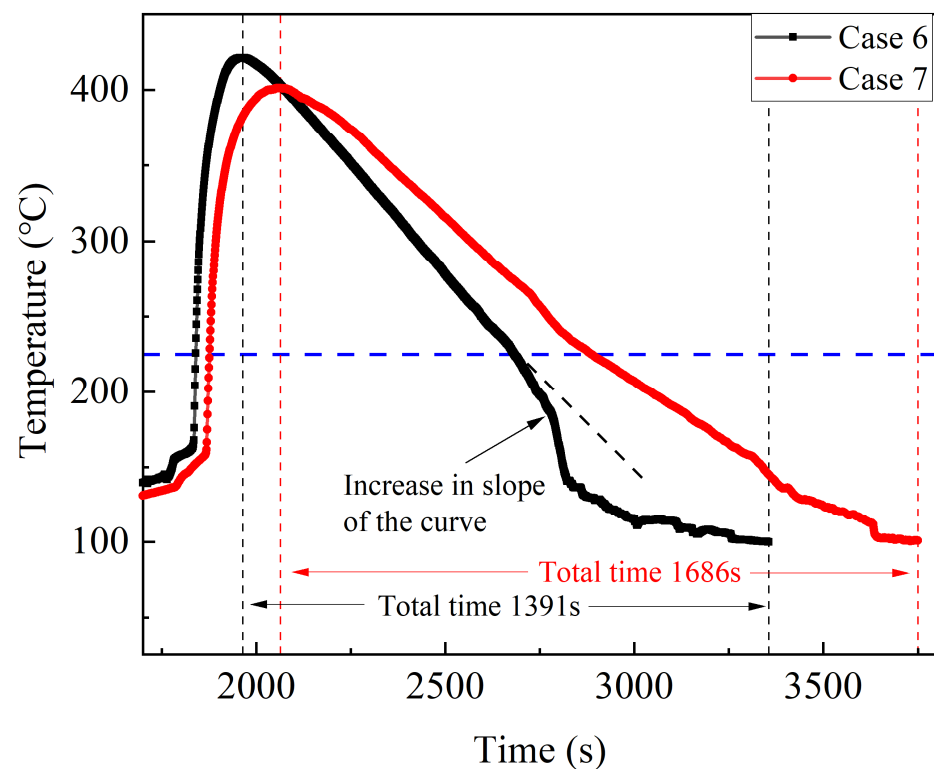


Figure 7. Cooling process curves at the end of thermal runaway of cells in Cases 6 and 7: (a) temperature curves; (b) cooling rate curves. (The blue line represents a battery temperature of 225 °C).

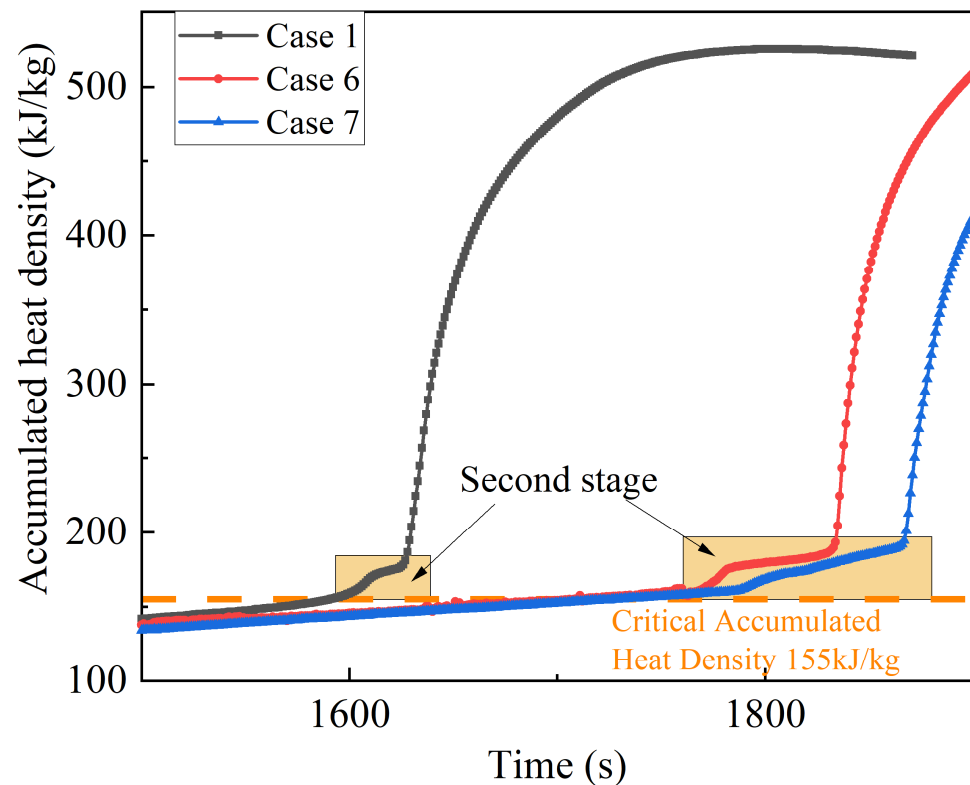


Figure 8. Variation curves of accumulated heat density of batteries for Cases 1, 6 and 7. (The yellow line represents the critical accumulated heat density).

3.2. Analysis of Water Mist against Thermal Runaway Flames

During thermal runaway, the active materials inside the lithium-ion battery will undergo a violent pyrolysis reaction. During the material pyrolysis process, a certain amount of H_2 , CO , CO_2 and hydrocarbon gases are generated, of which H_2 accounts for more than 99% [25], and the electrolyte is evaporated rapidly due to the considerable heat generated from the battery. During thermal runaway, a large amount of high-temperature greyish-white smoke is ejected from the safety valve at a high speed, and sometimes the battery flame extinguishes because the smoke is ejected too fast and mixes unevenly with the air. After the thermal runaway is initiated, a turbulent flame is formed above the safety valve. When applying water mist during this time, an obvious confrontation phenomenon between the water mist and the flame can be observed. This means the water droplets are unable to fall on the battery surface normally, which causes a reduction in cooling efficiency.

Figure 9 depicts the flame temperature and the change rate curve above the safety valve in Cases 6 and 7 during thermal runaway, of which the upper half of Figure 9a shows the temperature curve at the slightly higher flame temperature in Case 6 and the lower half the temperature curve at the slightly lower flame temperature, and the dotted line is the time of water mist release in Case 6. Upon the release of water mist, the temperature at 30 cm and 50 cm above the safety valve in Case 6 decreases rapidly, and the temperature increases rapidly with the intensifying combustion and is higher than that in Case 7; the temperature at 70 cm above the safety valve also shows a tendency to decrease followed by a rapid increase, but the temperature here is lower than that in Case 7; the temperature at 90 cm above the safety valve decreases rapidly and remains stable. It happens because when the thermal runaway is initiated, the gas ejection speed of the safety valve gradually increases, and the water mist gradually becomes unable to suppress the turbulent flame ejected at a high speed, and the flame height gradually increases. The pressure of water mist compresses the top of the flame, and the heat carried by the flame is also compressed below the distortion region, and the temperature of the flame in this region is also higher due to the heat storage; the distortion region of the flame is affected by the cooling of water

mist, and the overall temperature is lower than that of the non-extinguishing case, although the temperature increases faster in the development of thermal runaway; the temperature in the flame distortion region is maintained at a lower level due to the continuous cooling of water mist. It could therefore be determined that the flame distortion region is the region where the water mist confronts with the thermal runaway flame. The temperature is stable at a lower level above this region, and fluctuates greatly due to the flame fluctuation and the confrontation in this region. Compared to the non-extinguishing case, in this region the temperature is lower. However, in the immediate vicinity below this region, the temperature is higher and flame is more intense [26]. Figure 9b shows the variation curves of the temperature rise rate in the flame rise stage after the release of water mist, and the temperature rise rate is higher at 30 cm, 50 cm and 70 cm above the safety valve in Case 6. It is noted that for Case 6, although there is no high temperature section, the temperature rise rate is higher in the low temperature section at 70 cm, and both the temperature and the temperature rise rate are higher at 50 cm. The impact of water mist on flames can be divided into two main parts: one is to cool the heat at the top of the flame, suppressing the high temperature in the confrontation region; the other is to compress a proportion of the heat in the confrontation region, increasing the rate of temperature rise in the low-temperature region and the temperature as well as the rate of temperature rise in the adjacent regions below. Assuming that the batteries have the same rate of jet heat production at the same height and at the same moment of thermal runaway, the rate of heat change in the confrontation region and the adjacent region below is shown in Equations (9) and (10):

$$\dot{Q}_{zone} = \dot{Q}_{prod} - \dot{Q}_{WM} - \dot{Q}_{comp} \quad (9)$$

$$\dot{Q}_{zone-} = \dot{Q}_{prod} + \dot{Q}_{comp} \quad (10)$$

where \dot{Q}_{zone} and \dot{Q}_{zone-} are the rate of heat change in the confrontation region and the adjacent region below, respectively; \dot{Q}_{prod} is the rate of heat production in each region; \dot{Q}_{WM} is the rate of cooling by the water mist; \dot{Q}_{comp} is the rate of heat change compressed by the water mist.

The region with the highest flame fluctuation is identified as the confrontation region between the water mist and the thermal runaway flame. This region shows the highest fluctuation of the temperature rise rate in each period. The temperature increase rate curves at different points above the safety valve for Case 6 are shown in Figure 10. It is evident that the confrontation region initially rises and then decreases during the thermal runaway process. When the water mist is released, the confrontation region is at 30 cm above the safety valve, and it subsequently rises to 50 cm and 70 cm after 15 s and 35 s, respectively. Around 20 s later, the confrontation region gradually drops to 50 cm and stabilizes below 30 cm after 25 s, and the flame is extinguished after 44 s. During the development of thermal runaway, the height of the confrontation region tends to rise slowly from 30 cm to a maximum of 70 cm, then falls back and stabilizes for a long time at 50 cm, and finally falls more rapidly until the flame is extinguished. The reason for it is, in the thermal runaway process, the reaction rate inside the battery quickly reaches its peak and remains stable, and after a while the internal active material decreases so that the reaction rate decreases faster. The confrontation region in this case remains at 50 cm for most of the time, accounting for 40.4%. The flame morphology illustrated in Figure 11 is affected the most by the confrontation: at this stage, the safety valve gas jet speed increases, so that the upward force generated by the flame jet increases, and gradually matches the downward force of the water mist. As the gas pressure decreases with increasing height, the flame flow rate is high at the bottom and low at the top, the flame width is small at the bottom and large at the top, and the flame morphology is also "conical". At a distance of 30 cm, the jet speed of the safety valve is too low, so that the flame cannot fight against water mist, and the flame morphology is shown as "stacked"; at a distance of 70 cm, on the other hand, the jet speed of the flame is too high, so that the water mist can only suppress a small region at the top

of the flame, and the flame morphology is shown as “T-shaped”. Compared with Case 7, the water mist primarily affects the flame morphology in other periods, except when the thermal runaway reaches the peak: before the thermal runaway reaches the peak, the flame height could be compressed to a certain extent; after the thermal runaway reaches the attenuation period, the flame height could be compressed and the flame extinguishing could be accelerated.

According to the heat calculation table in Chapter 3.1, the heat removed from the battery by the water mist in Cases 6 and 7 is 580.3 kJ and 592.1 kJ, respectively, and the heat remaining in the battery at the end of the thermal runaway in the two cases is 756.2 kJ and 880.4 kJ, respectively. Assuming that the total heat production during thermal runaway is the same in the two cases, the difference in the remaining heat at the end of thermal runaway is 124.2 kJ, which is the cooling amount of water mist during the thermal runaway period, so the total cooling amount of water mist in Case 6 could be divided into two parts, 124.2 kJ during the thermal runaway period and 456.1 kJ after the thermal runaway. It indicates that during thermal runaway, the cooling amount of water mist accounted for 21.4% of the total cooling, and the cooling rates of the two parts are 0.57 kW and 0.33 kW, respectively. In Case 6, the cooling duration in thermal runaway accounts for only 13.5% of the total cooling, and the cooling duration after the end of thermal runaway is 295 s shorter than that in Case 7. This suggests that while the long release distance challenges the water mist in its ability to fight against the thermal runaway flame, and the water droplets could not normally fall on the battery surface and inhibit the development of thermal runaway, it could still maintain a better cooling effect and reduce the damage of thermal runaway and the difficulty of subsequent cooling.

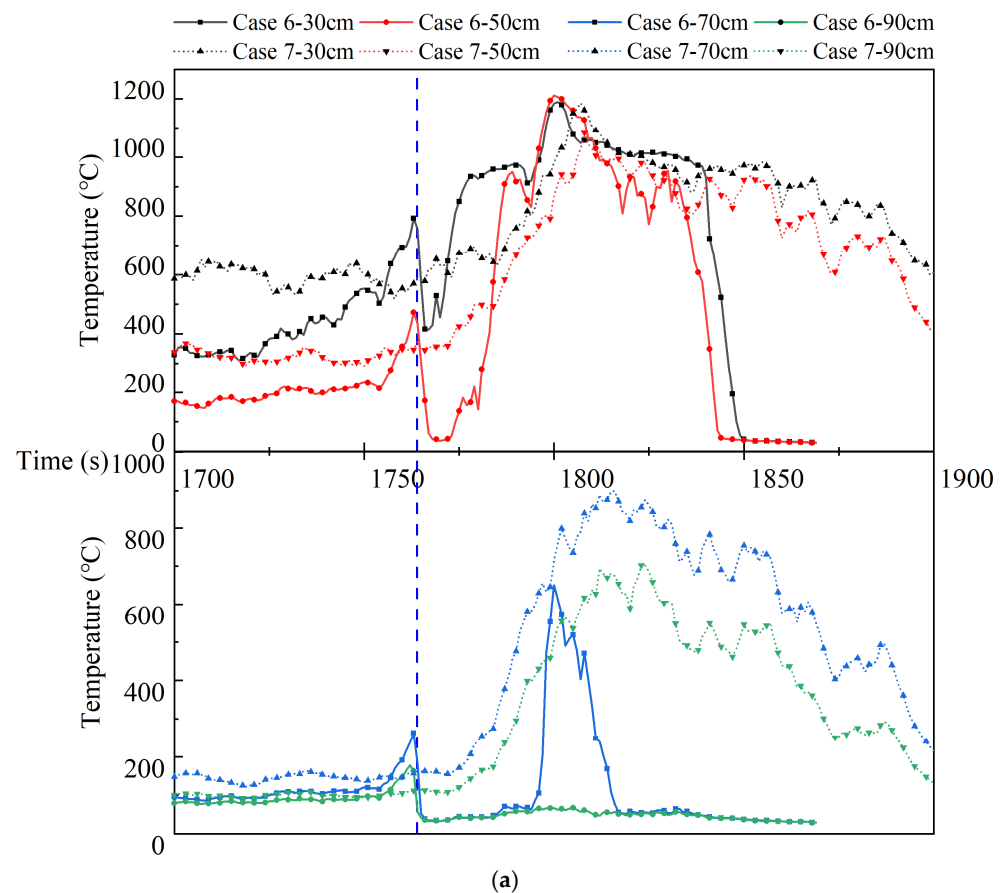


Figure 9. Cont.

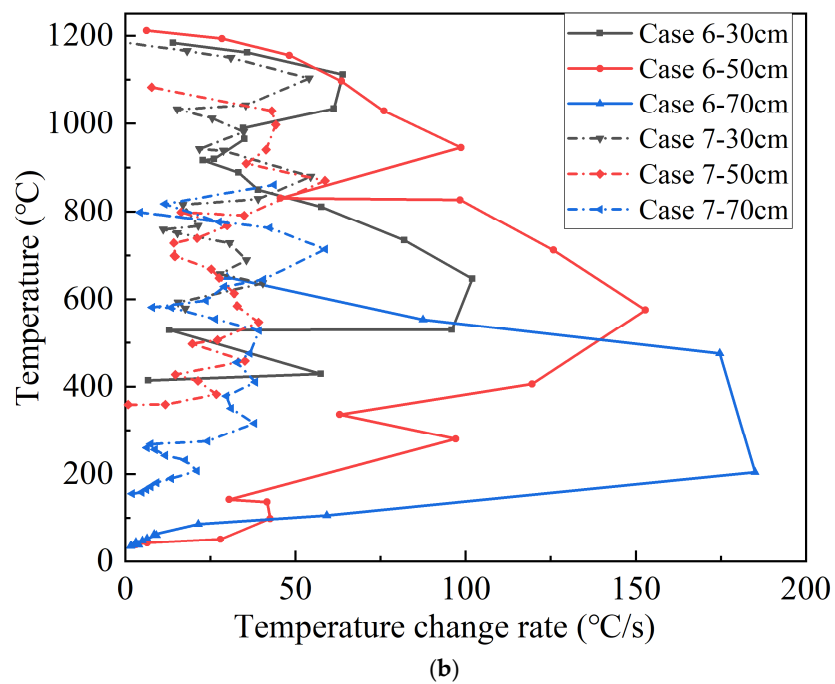


Figure 9. Flame temperature and rate of change curve of thermal runaway safety valve for Cases 6 and 7: (a) temperature; (b) temperature change rate. (The blue vertical line represents the water mist release time point).

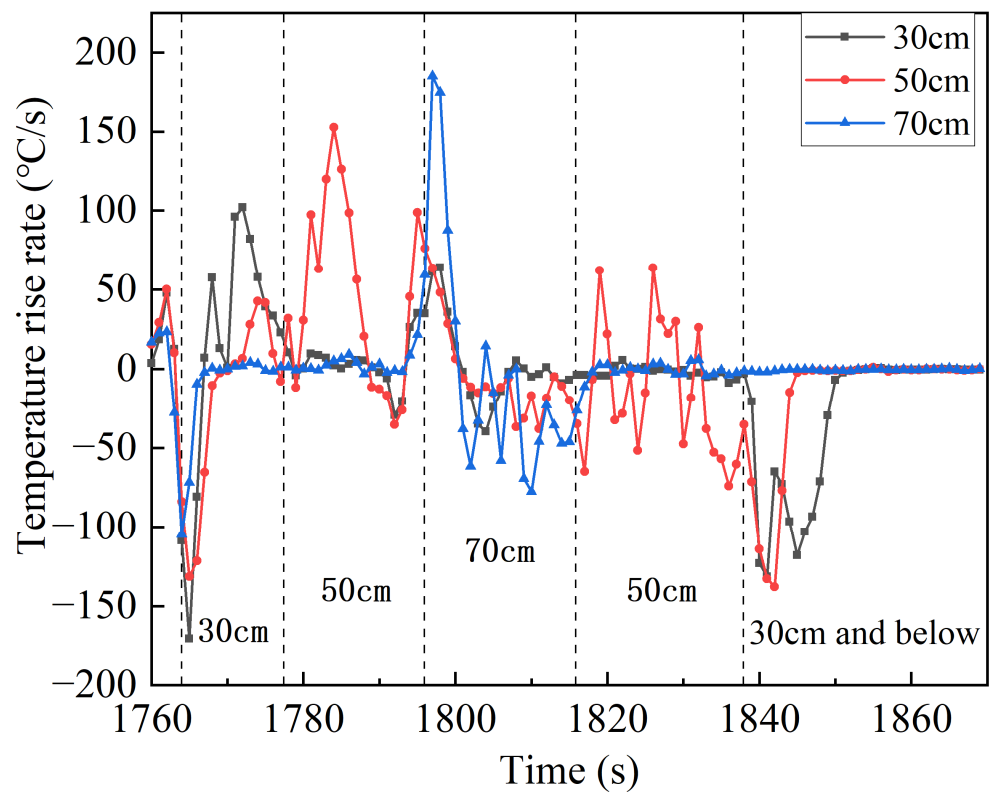


Figure 10. Temperature rise rate curves at various locations above the safety valve for Case 6.

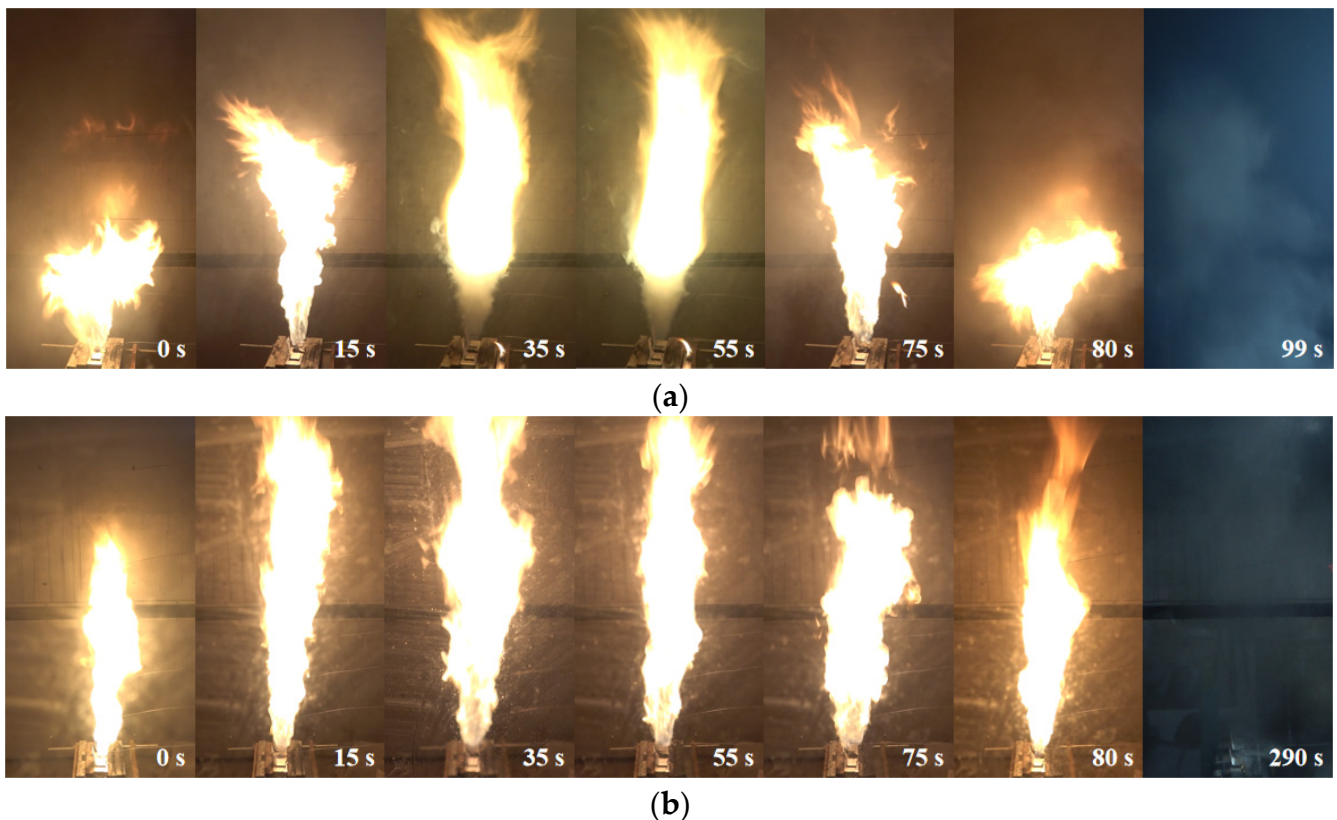


Figure 11. Thermal runaway flame morphology for Cases 6 and 7: (a) Case 6; (b) Case 7.

4. Conclusions

(1) In the case of thermal abuse of a 100 Ah square LiFePO_4 battery, the release of water mist before the initiation of thermal runaway could inhibit the development of thermal runaway, and the cooling effect is better after the opening of the battery safety valve, and the cooling rate is improved by more than 10 times compared with the unopened case. Once thermal runaway has been initiated, water mist cannot prevent the development of thermal runaway, but it could significantly shorten the total duration of thermal runaway and reduce the cooling time after thermal runaway.

(2) The use of water mist could only inhibit the development of thermal runaway until the battery reaches a critical accumulated heat density of 155 kJ/kg. After exceeding this point, due to the irreversible damage to the internal structure of the battery, water mist cannot suppress the fire, but could only shorten the duration of thermal runaway and the cooling time required after thermal runaway, thus reducing the losses.

(3) During thermal runaway of the battery, a phenomenon is observed where water mist is fighting against the flame. The impact of the confrontation primarily involves two parts: first is to cool the heat of the flame at the top, inhibit the high temperature in the confrontation region; second is to compress part of the heat in the confrontation region, increase its low-temperature temperature rise rate and its adjacent region of temperature and temperature rise rate below. The confrontation affects the morphology of the flame 50 cm above the safety valve the most, with the flame forming a “cone” with a small bottom and a large top. Although the water mist droplet could not fall properly on the surface of the battery due to the confrontation effect, it could still maintain a good cooling rate of 0.57 kW.

Author Contributions: Conceptualization, G.L.; methodology, X.M.; software, W.S.; writing—original draft preparation, X.H.; writing—review and editing, T.L.; supervision, T.L.; project administration, J.Y.; funding acquisition, Q.L. and G.Z. All authors have read and agreed to the published version of the manuscript.

Funding: This research was funded by Opening Fund of State Key Laboratory of Fire Science grant number [No. HZ2023-KF02], the Central University Basic Research Fund of China [No. 2022ZZCX05K05], and the APC was funded by the Scientific Project of State Grid Tianjin Electric Power Company [No. ki22-1-30].

Data Availability Statement: All data included in this study are available upon request by contact with the corresponding author.

Acknowledgments: This work was supported by Opening Fund of State Key Laboratory of Fire Science (SKLFS) under Grant (No. HZ2023-KF02), the Central University Basic Research Fund of China (No. 2022ZZCX05K05) and the Scientific Project of State Grid Tianjin Electric Power Company (No. kj22-1-30).

Conflicts of Interest: The authors declare no conflict of interest.

References

1. Ping, M.I.; Zhen, Y.A.; John, L.E.; Qinghua, L.I.; Baoguo, W.A. Current situations and prospects of energy storage batteries. *Energy Storage Sci. Technol.* **2020**, *9*, 670–678.
2. Peng, X. Patent Analysis of Cathode Materials for Ternary Lithium Ion Batteries. *World Nonferrous Met.* **2022**, *18*, 162–164.
3. Wang, B.; Zhang, X. *Lithium Battery and Its Safety*; Metallurgical Industry Press: Beijing, China, 2022; pp. 58–60.
4. Qi-Yu, W.; Shuo, W.; Ge, Z.; Jie-Nan, Z.; Jie-Yun, Z.; Xi-Qian, Y.; Hong, L. Progress on the failure analysis of lithium battery. *Acta Phys. Sin.* **2018**, *67*, 128501.
5. Diaz, F.; Wang, Y.; Weyhe, R.; Friedrich, B. Gas generation measurement and evaluation during mechanical processing and thermal treatment of spent Li-ion batteries. *Waste Manag.* **2018**, *84*, 102–111. [[PubMed](#)]
6. Zou, K.; He, K.; Lu, S. Venting composition and rate of large-format LiNi_{0.8}Co_{0.1}Mn_{0.1}O₂ pouch power battery during thermal runaway. *Int. J. Heat Mass Transf.* **2022**, *195*, 123133. [[CrossRef](#)]
7. Liu, Y.; Niu, H.; Xu, C.; Huang, X. Thermal runaway propagation in linear battery module under low atmospheric pressure. *Appl. Therm. Eng.* **2022**, *216*, 119086.
8. Zhang, Q.; Niu, J.; Zhao, Z.; Wang, Q. Research on the effect of thermal runaway gas components and explosion limits of lithium-ion batteries under different charge states. *J. Energy Storage* **2022**, *45*, 103759. [[CrossRef](#)]
9. Zhang, L.; Jin, K.; Sun, J.; Wang, Q. A Review of Fire-Extinguishing Agents and Fire Suppression Strategies for Lithium-Ion Batteries Fire. *Fire Technol.* **2022**, 1–42. [[CrossRef](#)]
10. Ma, B.; Lin, C.; Liu, L.; Ma, X.; Ma, T.; Liu, S. Venting characteristics and flammability limit of thermal runaway gas of lithium ion battery. *Energy Storage Sci. Technol.* **2022**, *11*, 1592–1600.
11. Li, Y.; Yu, D.; Zhang, S.; Hu, Q.; Liu, X.; Wang, J. On the fire extinguishing tests of typical Lithium-ion battery. *J. Saf. Environ.* **2015**, *15*, 120–125.
12. Rao, H.; Luo, X.-F.; Liu, A.; Wang, Z.-H.; Xi, Q.; Zhang, Z. Study on comparative fire extinguishing tests between ternary lithium battery cabin and lithium iron phosphate battery cabin of electric ships. *Fire Sci. Technol.* **2021**, *40*, 433–437.
13. Xu, J.; Guo, P.; Duan, Q.; Yu, X.; Zhang, L.; Liu, Y.; Wang, Q. Experimental study of the effectiveness of three kinds of extinguishing agents on suppressing lithium-ion battery fires. *Appl. Therm. Eng.* **2020**, *171*, 115076.
14. Zhang, L.; Li, Y.; Duan, Q.; Chen, M.; Xu, J.; Zhao, C.; Sun, J.; Wang, Q. Experimental study on the synergistic effect of gas extinguishing agents and water mist on suppressing lithium-ion battery fires. *J. Energy Storage* **2020**, *32*, 101801.
15. Zhang, L.; Duan, Q.; Liu, Y.; Xu, J.; Sun, J.; Xiao, H.; Wang, Q. Experimental investigation of water spray on suppressing lithium-ion battery fires. *Fire Saf. J.* **2021**, *120*, 103117.
16. Liu, T.; Liu, Y.; Wang, X.; Kong, X.; Li, G. Cooling control of thermally-induced thermal runaway in 18,650 lithium ion battery with water mist. *Energy Convers. Manag.* **2019**, *199*, 111969.
17. Liu, T.; Hu, J.; Tang, Q.; Zhu, X.; Wang, X. Mitigating overcharge induced thermal runaway of large format lithium ion battery with water mist. *Appl. Therm. Eng.* **2021**, *197*, 117402.
18. Liu, T.; Tao, C.; Wang, X. Cooling control effect of water mist on thermal runaway propagation in lithium ion battery modules. *Appl. Energy* **2020**, *267*, 115087.
19. Li, L.; Zhang, B.; Sun, Z.; Chen, M. Study on the inhibition effect of additive water mist on the thermal runaway of aged lithium-ion batteries. *Fire Sci. Technol.* **2023**, *42*, 79–83.
20. Liu, Y.; Duan, Q.; Xu, J.; Li, H.; Sun, J.; Wang, Q. Experimental study on a novel safety strategy of lithium-ion battery integrating fire suppression and rapid cooling. *J. Energy Storage* **2020**, *28*, 101185. [[CrossRef](#)]
21. Hu, Z. Experimental Investigation of Steel and Aluminum Alloy Surface Emissivity Characteristics. Master's Thesis, Henan Normal University, Xinxiang, China, 2010.
22. Zhu, L.; Xu, X.; Zhao, L.; Yuan, Q. Comparative analysis of thermal runaway characteristics of lithium-ion battery under oven test and local high temperature. *Fire Mater.* **2022**, *46*, 397–409. [[CrossRef](#)]
23. Li, H.; Duan, Q.; Zhao, C.; Huang, Z.; Wang, Q. Experimental investigation on the thermal runaway and its propagation in the large format battery module with Li(Ni_{1/3}Co_{1/3}Mn_{1/3})O₂ as cathode. *J. Hazard. Mater.* **2019**, *375*, 241–254.

24. Ouyang, C.; Liang, B.; Liu, Y. Progress of thermal safety characteristics of high power lithium-ion batteries. *Chin. J. Power Source* **2014**, *38*, 4.
25. Galushkin, N.E.; Yazvinskaya, N.N.; Galushkin, D.N. Mechanism of thermal runaway in lithium-ion cells. *J. Electrochem. Soc.* **2018**, *165*, A1303.
26. Parekh, M.H.; Li, B.; Palanisamy, M.; Adams, T.E.; Tomar, V.; Pol, V.G. In situ thermal runaway detection in lithium-ion batteries with an integrated internal sensor. *ACS Appl. Energy Mater.* **2020**, *3*, 7997–8008.

Disclaimer/Publisher's Note: The statements, opinions and data contained in all publications are solely those of the individual author(s) and contributor(s) and not of MDPI and/or the editor(s). MDPI and/or the editor(s) disclaim responsibility for any injury to people or property resulting from any ideas, methods, instructions or products referred to in the content.